Chapter 3

Low pressure and scaling properties

3.1 Introduction

The theory presented in part I addresses the thermostatistics of "small" systems. This thermostatistics has already been applied to many models covering a wide range of physical domains. Historically, one of its firsts applications, were linked to the study of "liquid–gas" phase transitions of hot nuclei and metallic clusters composed of a few hundreds of particles or atoms, see e.g. [GRO90, GH95, GM97]. For those systems there is no heat–bath, and they exhibit properties that are absent in the limit $N \to \infty$.

In this part, the study of the equilibrium properties of the transition from (liquid) sodium [a] clusters composed of 50 up to 5000 atoms to gases of atoms as functions of the microcanonical pressure and of the total excitation energy is presented. This work continues the one done by Gross at al., e.g. [GMS97, MHGS97, SKM$^+$97, GM97].

In previous applications of the microcanonical thermodynamics for small systems the numerical works were based on MMMC, the Microcanonical-Metropolis-Monte-Carlo sampling. It is a method that samples the accessible *microcanonical* phase space of N–body systems [ZGXZ87], rather than performing dynamical computations, e.g. [BBG97]. In MMMC, contrary to dynamical calculations, there is no need to follow every single degree of freedom (see below). One of the key feature of MMMC is that it explores the partitioning phase–space without any *a priori* assumption about the mass distribution (in contrast with e.g. an evaporation model). Practical applications of MMMC already gave good qualitative and quantitative results and shed new lights onto the problems of coulomb explosions of metallic clusters [SKM$^+$97, SCH97] and on their liquid–gas phase transition. The main outcome of these works is, in complete analogy with the nuclear application of MMMC [b], the prediction of a first order phase transition and of a multifragmentation regime within a certain range of energies [GM97]. The nuclear model and the cluster model have both a multifragmentation regime although the physical reasons that lead to this regime are different. In the cluster case, the multifragmentation is mainly induced by the electronic shell effects (see below). Whereas, in the nuclear case, the coulomb repulsion of the uniformly distributed charges plays a major role. The multifragmentation regime, the mass

[a] Sodium has been chosen since it is experimentally well explored, and a lot of material data are available, e.g. [FL95].

[b] In the following, the cluster and nuclear *models* which use the MMMC *method* are also noted by MMMC.

distribution is characterized by the presence of many intermediate mass fragments (see below). This regime vanishes in the limit $N \to +\infty$.

One of the first aim of the work presented in this thesis was to study the liquid–gas phase transition of small metallic clusters at high pressure up to eventually the critical point as defined in chap. 2 (if it exists at all) and to study whether and how precursors of critical behaviors show up (e.g. mass distribution described by a power law, infinite correlation lengths [c], etc). Another goal was to explore in details this phase transition at low pressures.

In order to achieve this program the old code implementing the MMMC method on the cluster model [d] was rewritten from scratch for several reasons, e.g.

- MMMC77 uses an approximation in order to estimate NCC, a quantity linked to the avoided volume (see below and app. A), which is far from being valid and useful at high pressures.
- The algorithm to sample the mass partition fulfills the detailed balance only "on average" in MMMC77 [GM87, ZGXZ87, GRO97]. At low pressure, this approximation is in most of the cases sufficient. But, since huge fluctuations in the mass distribution can be expected near the critical point, it is safer to implement a correct sampling that fulfills "locally" the detailed balance equation (see app. B.2.1).
- Finally, some new improvement to the model had to be incorporated in the code, especially regarding the model of the internal entropy of the clusters.

The rest of this chapter is organized as follow. In section 3.2 the cluster model is introduced. Then, the MMMC method is briefly presented in sec. 3.3. More technical "details" are left for the appendices A and B. In section 3.4 the numerical results on the liquid–gas transition of small clusters of sodium at atmospheric pressure are presented and discussed [e]. First, for a system composed of two hundreds atoms in sec. 3.4.1. Then, the scaling behavior of the mass distributions and of the transition parameters are discussed in sec. 3.4.2. Results on the liquid–gas transitions of sodium clusters based on MMMC77 have already been published in e.g. [GMS97, MHGS97, SKM$^+$97, GM97]. In sect. 3.4 some of these results (noted hereafter [GM] or [GM97]) are compared with the ones of the present thesis. The results are collected and summarized in section 3.5.

3.2 Model

The MMMC cluster model has been described in many papers and reviews [GRO97, SCH97]. Hence hereafter, only the basic assumptions are recalled with a particular stress on the differences between the "old" and the "new" model [f].

The aim of MMMC is to sample the phase space accessible to a model for metallic clusters [g] and to get information about the derivatives of its entropy and about its mass distribution. It is a *microcanonical* model, thus the "extensive" parameters of the model as defined in part I are conserved.

[c] Of course in finite size systems the correlation lengths can only be very large, and the mass distributions are described by power laws over a finite range of masses.

[d] Hereafter, the previous and the new codes are noted MMMC77 and MMMC95, respectively.

[e] High pressures studies are presented in chap. 4.

[f] Throughout this section atomic units are used, i.e. $\hbar = m_e = e = 4\pi\epsilon_0 = 1$

[g] In the present work only *uncharged* sodium clusters are considered.

System

The system is composed by a spherical container whose volume is fixed and equal to $V = \frac{4\pi}{3}R^3$ and of A atoms of sodium. These atoms can be bounded and form clusters. Inside this container, the clusters are positioned (they must fit within V). Neither the number of clusters N_f nor the mass distributions are restricted, provided again, that they satisfy the microcanonical constraints and fit within the container.

The container breaks the translational symmetry. Therefore, the total linear momentum $\mathbf{P}$ is not conserved. In order to avoid a dependence of the results on the box-shape, the total angular momentum $\mathbf{L}$ is also considered as free to fluctuate [h]. The conserved quantities are the total number of atoms A, the volume V and the total energy E.

Clusters

The clusters are modeled in the following way:

1. All clusters are assumed to be *spherical hard spheres* [i]. Their individual volume v_i is $v_i = \frac{4\pi}{3}N_i r_w^3 = \frac{4\pi}{3}R_i^3$ where r_w is the Wigner–Seitz radius, N_i the number of atoms of the cluster i and R_i its radius. Hence, all clusters have the same density.

2. The mass m_i of a cluster of size N_i is given by $m_i = m_0 N_i$ where m_0 is the mass of a monomer (atom) [j,k]. The total mass of the system M is given by $M = A\, m_0$.

3. The binding energy of a cluster $E_{b\,i}$ is a function of its mass [l] N_i. For clusters of mass within the range $[2, 21]$ the binding energies are taken from experimental data [KSR+88]. For $N_i > 21$, the classical metallic–drop model is used. For the ground–state binding energy this model gives

$$E_{b\,i} = -a_v N_i + a_s N_i^{2/3}, \tag{3.1}$$

   where a_v and a_s are two positive coefficients related to the volume and to the surface energy, see fig. 3.1 on the following page.

4. The eigen–rotation of a cluster with $N_i > 2$ is treated classically. For dimers and trimers their geometrical structures are taken explicitely. As a dimer is a linear molecule, only two angles are required in order to determine its orientation in space (three angles are needed for $N_i > 2$). Its principal moment of inertia are $I_1 = I_2 = \frac{1}{2}m_0 d^2$, $I_3 = 0$, where d is the dimer bond length. For a trimer, the principal moment

[h] In the previous MMMC model, there was no real container, but a freeze–out volume within which the system was assumed to equilibrated before escaping this volume. This was closely related to the experiments, since in experimental cluster physics the systems are open [GRO97]. Consequently $\mathbf{P}$ and $\mathbf{L}$ were conserved quantities. Here, a real volume is needed to make the concept of pressure sensible.

[i] In the previous model, the monomers were allowed to overlap with other clusters (other monomers included). This was a way to simulate highly excited clusters. I.e. clusters whose internal excitation energies are well above maximal allowed specific internal excitation energy ϵ^*_{max} (see below). For practical reasons, this is not included in the present model. This decision is supported a posteriori by the fact that, in all the performed simulations, the internal excitation energy of the clusters were seldomly close to ϵ^*_{max} (see below).

[j] As the mass of a cluster is proportional to its number of atoms and for simplicity, N_i is in the following a short hand for the number of atoms but also for the mass of cluster i.

[k] To avoid cumbersome notations, the monomers are also called "clusters".

[l] For a monomer $E_{b\,i} = 0$.

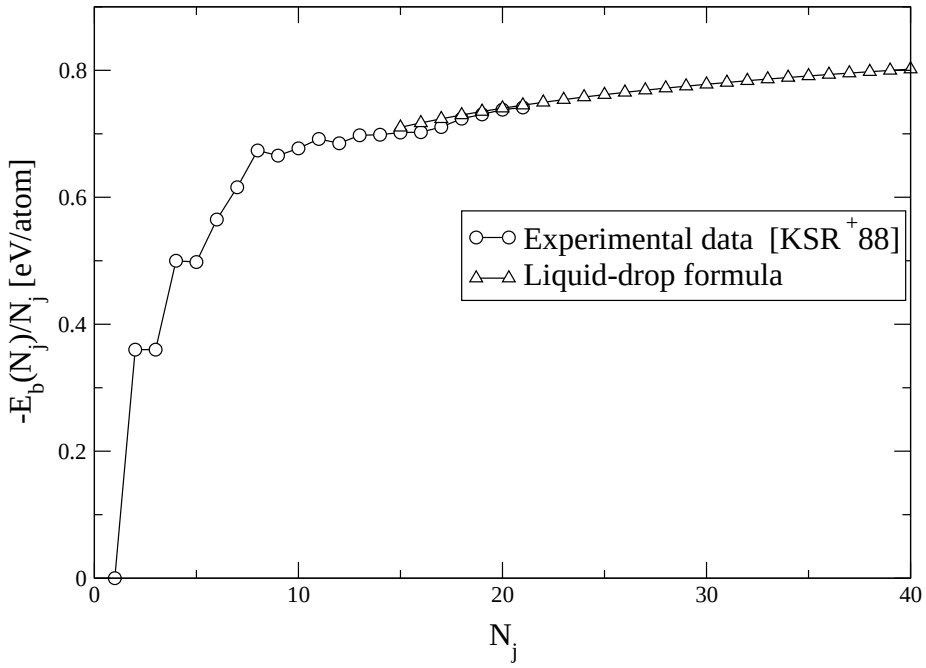

Figure 3.1: Specific binding energy as a function of the cluster size: experimental data [KSR$^+$88] and liquid–drop formula with $a_v = 1.039$ eV [BCC$^+$90, BCC$^+$95] and $a_s = 0.8109$ eV. Note that the value of a_s is experimentally known with a large uncertainty (see [GM97] and refs. quoted therein). Here, a_s is adjusted to obtain the best fit with the experimental data. Note also the local maxima of E_b/N_j at $N_j = 2$, 4, 8 and 12 due to the electronic shell effects.

of inertia are determined assuming a triangular geometry. The clusters with $N_i > 4$ are regarded as classical homogeneous spherical body. Their principal moment of inertia are given by $I_1 = I_2 = I_3 = \frac{2}{5} N_i m_0 R_i^2$.
The monomers have a spin degeneracy of 2.

5. Clusters ($N_i > 1$) have internal degrees of freedom (dof). The internal excitation energy of cluster i is noted by E_i^*. For the dimers and the trimers, it is assumed that the internal dofs are well described by quantum Einstein models. Moreover, the internal excitation energy for dimers and trimers are upper bounded by their respective dissociation energies D_d and D_t.

   (a) A dimer has one internal dof which is associated with one quantum harmonic oscillator having a frequency ω_d. The discrete energy levels are given by $E_i^* = \left(k_1 + \frac{1}{2}\right) \hbar\omega_d$ where $k_1 \in \mathbb{N}$. These levels are not degenerate, so in this model, a dimer carries no internal entropy.

   (b) A trimer is a non–linear molecule with three internal dofs which are associated with three independent distinguishable quantum harmonic oscillators having all the same frequency ω_t. The energy levels E_i^* are given by $E_i^* = \left(k_1 + k_2 + k_3 + \frac{3}{2}\right) \hbar\omega_t$, where $k_1, k_2, k_3 \in \mathbb{N}$. The degeneracy number n_t of an

energy level is given by $n_t(E_i^*) = \frac{1}{2}\left(\frac{E_i^*}{\hbar\omega_t}\right)^2 - \frac{1}{8}$. The internal entropy of a trimer is simply

$$S_t(E_i^*) = \ln n_t(E_i^*). \tag{3.2}$$

(c) In the previous model, clusters with $N_i > 3$ did not have an individual excitation energy but, on contrary, an overall E^* was assigned to all those clusters. I.e. they were considered as one unique big fragment. Or in other words, all their internal dofs had the same specific excitation energy. Moreover, as there is no available data on the entropy for *all cluster sizes*, the functional form of the entropy of this "overall" cluster was taken from the bulk.
In the new version, all clusters have their own internal excitation energy E_i^*. This energy takes its values within the range $[0, N_i^*\epsilon_{max}^*]$ where $\epsilon_{max}^* \approx 0.35\ \frac{\text{eV}}{N^*}$ is the maximum specific internal energy [m] and $N_i^* = N_i - 2 = \frac{3N-6}{3} = \frac{\text{internal dofs}}{3}$. Here, it is assumed that 3 degrees of freedom represent together one bulk atom [GRO97]. Furthermore, in order to include some surface effects to the expression of the internal entropy S_int and to have a smooth specific entropy $s_{int} = S_{int}/N^*$ as a function of $\epsilon_i^* = E_i^*/N^*$ *and* N^* from $N^* = 3$ to $N^* \to \infty$ the following model is assumed

$$S_{int}(\epsilon^*, N^*) \doteq N_s^* s_t(\epsilon^*) + N_v^* s_\infty(\epsilon^*), \tag{3.3}$$

where s_t and s_∞ are the trimer and the bulk specific entropies. N_s^* and N_v^* are the number of surface and volume "atoms", respectively.
s_t is given by eq. (3.2). s_∞ is computed from the experimental specific heat capacity at constant pressure $c_p(T)$ [FL95] (for further and detailed explanations see e.g. [GRO97]). In fig. 3.2 the specific heat capacity at constant pressure $c_p(T)$ is plotted at atmospheric pressure and the specific entropy and the temperature versus ϵ are shown on fig. 3.3. It is worth to notice that the bulk remains in the liquid phase up to a specific energy of $\epsilon_{max}^* \approx 0.35$ eV/atom.

The number N_s^* of surface atoms are estimated in the following way (see fig. 3.4 on page 45). Consider a cluster of diameter R_i. Its surface fragments are approximatively inside an external layer of thickness $\approx 2r_w$ (the diameter of a monomer). The volume of this layer is V_s and the number of surface atoms is $\sim \frac{V_s}{v_0}$ where v_0 is the monomer volume (eigen–volume), i.e. $v_0 = \frac{4\pi}{3}r_w^3$, it follows

$$N_v^* = \max\left(0, N^* - 6N^{*\,2/3} + 12N^{*\,1/3} - 8\right), \tag{3.4a}$$

$$N_s^* = N^* - N_v^*. \tag{3.4b}$$

Fig. 3.5 on page 45 shows the specific entropy s at $\epsilon^* = 0.35\text{eV}/N^* = \epsilon_{max}^*$ along with the proportion of volume atoms $N_v^*/N^* = 1 - N_s^*/N^*$ as functions of N^*. There is no volume fragment for clusters of size $N = N^* + 2 < 14$; the number of surface fragments and therefore the relative weight of the surface entropy in the total cluster entropy is very important even for clusters composed of ten thousands atoms [n,o].

[m] In fact, the exact value of ϵ_{max}^* is not very constraining, as the results of the MMMC95 simulations depend only marginally on ϵ_{max}^*. The excitation energy of a given cluster is seldomly close to the limit $N_i^*\epsilon_{max}^*$, at least for the range of system total mass studied (see below).

[n] The largest system considered in this work is composed of 5000 atoms.

[o] $s_\infty(\epsilon^* = 0.35) \approx 11.7$.

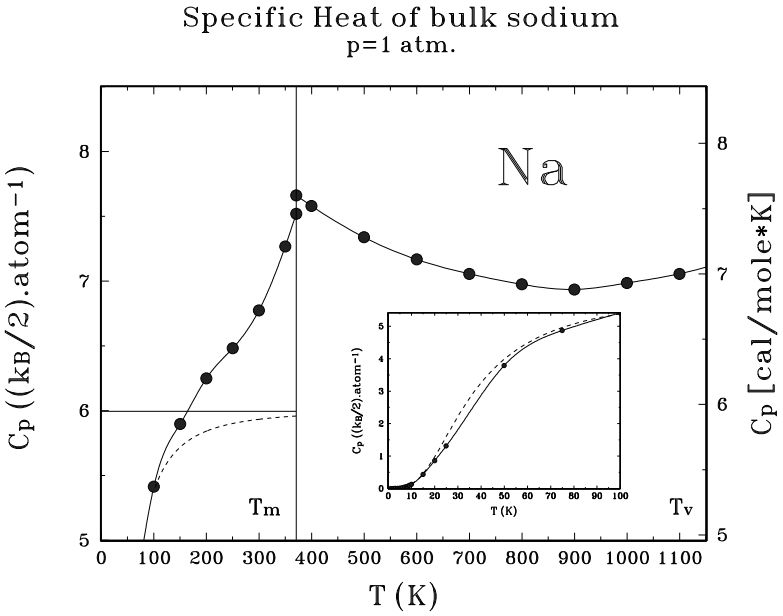

Figure 3.2: Specific heat capacity at constant (atmospheric) pressure of bulk sodium C_p [BOR63, HOAK63]. The dashed line represents the specific heat capacity calculated within the Debye model.

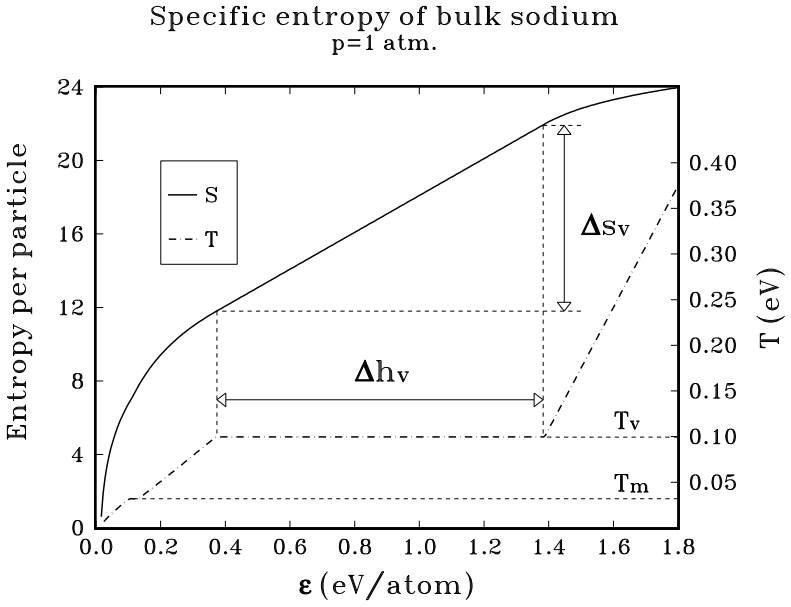

Figure 3.3: Specific entropy and temperature of bulk sodium at atmospheric pressure. Δh_v is the latent heat at constant pressure; T_m and T_v are resp. the melting and the vaporization temperatures.

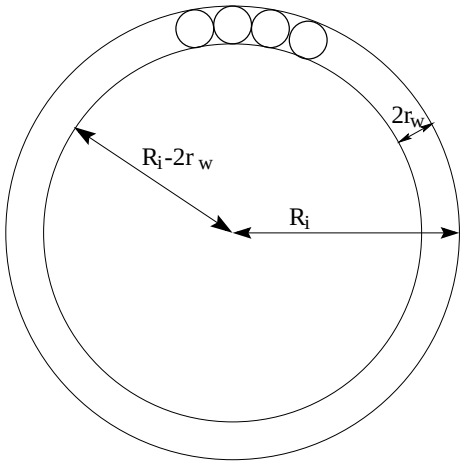

Figure 3.4: Schematic cluster model for the number of surface and volume degrees of freedom. R_i is the actual clusters radius and r_w is the Wigner-Seitz radius (radius of a monomer). The surface atoms are located on spherical shell of inner (outer) radius equal to $R_i - 2r_w$ (R_i).

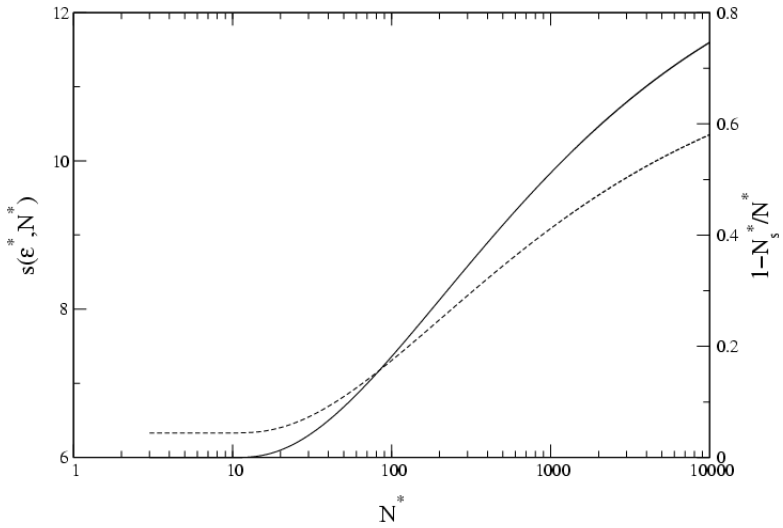

Figure 3.5: Entropy $s(\epsilon^* = 0.35\ \mathrm{eV/atom}, N^*)$ (dashed line; defined by eq. (3.3) on page 43) and proportion of volume "fragments" $N_v^*/N^* = 1 - N_s^*/N^*$ (plain line; defined by eq. (3.4b) on page 43) versus N^*. Within the present model the surface effects are very important for clusters as heavy as $A = 10^4$.

6. The polarization effects between the metallic clusters are neglected.

The simulation parameters used throughout part II are listed in table 3.1.

Total energy

The conserved total energy E is

$$E = E^* + E_k + E_r - E_b, \tag{3.5}$$

r_w (Å)	2.310
a_s (eV)	0.8109
a_v (eV)	1.039
ω_d (eV)	0.01490
ω_t (eV)	0.01048
d (Å^2)	2.67
I_2/m_0 (Å^2)	4.74
$I_{3,1}/m_0$ (Å^2)	4.84
$I_{3,2}/m_0$ (Å^2)	5.66
$I_{3,3}/m_0$ (Å^2)	10.49
D_d (eV)	0.72
D_t (eV)	0.36

Table 3.1: Experimental and theoretical values of the different parameters used in the calculations. r_w is the Wigner–Seitz radius at one atmosphere [FL95]; a_v is the volume cohesion energy and a_s its surface part (the value of a_s is adjusted in order to have a smooth binding energy per degrees of freedom for $15 \lesssim N \lesssim 31$, see fig. 3.1 on page 42) [BCC$^+$90, BCC$^+$95].; d is the dimer bond length [FID$^+$83]; the principal moment of inertia for the dimer I_2 and for the trimer I_3.

where $E_b = \sum_i E_{b\,i}$ and $E^* = \sum_i E_i^*$ are the total binding and internal energies (see items (3) and (5) on page 41). $E_k = \sum_i \frac{\mathbf{p}_i^2}{2m_i} + \sum_i \sum_{\nu=1}^{f_{ri}} \frac{l_{\nu\,i}^2}{2I_{\nu\,i}}$ is the sum of the total kinetic and total rotational energy, where $\mathbf{l}_i$ and $I_{\nu\,i}$, $i = 1, \ldots, f_{ri}$ are the angular momentum the principal moment of inertia,respectively and f_{ri} is the number of rotational dof (see item (4) on page 41). E_k is also called "remaining energy".

3.3 Simulation method

Microcanonical weight

MMMC is based on a Metropolis Monte–Carlo method [MRR$^+$53]. It builds a (Markovian) chain of states in the phase space accessible to the system. As in the microcanonical ensemble all microstates are accessible with the same probability the weight that should be used during the Metropolis test is the same for all microstates $\{\mathbf{q}, \mathbf{p}\}$ (see app. B.2). However some of the coordinates (dofs) are irrelevant in the sense that they are unobservable (e.g. internal degrees of freedom) and/or the observables of interest do not depend explicitely on those coordinates.

Therefore instead of working with the full generalized set of coordinates it is more reasonable to integrate, if possible, over the irrelevant (unobserved) coordinates. For the present model, the results of this integration gives the following new set of coordinates

$$\mathbf{x} \doteq \left\{ \mu = \{N_i\}_{i=1}^{N_f}, \{E_i^*\} \right\}, \tag{3.6}$$

where μ is a short hand for the mass distribution, and $\{E_i^*\}$ is the set of internal excitation energies (there are $N_f - N_m$ elements in this set, where N_m is the number of monomers in μ). The set over which $\mathbf{x}$ is defined is noted by W'.

Now in this set of coordinates the microcanonical density of states $\omega(\mathbf{x})$ is no longer uniform but equal to

$$\omega(\mathbf{x})\, d\mathbf{x} = \int_{\Omega} d\mathbf{q}\, d\mathbf{p} \delta\left(X\left(\{\mathbf{q},\mathbf{p}\}\right) - X_0\right) \delta\left(\mathbf{x}\left(\{\mathbf{q},\mathbf{p}\}\right) - \mathbf{x}\right), \tag{3.7}$$

where $X_0 = \{E, N, V\}$ is the set of "extensive" conserved quantities.

The detailed derivation of the microcanonical weight for the fragmentation phase space of atomic clusters can be found in refs. [GROB, GH95].

$\omega(\mathbf{x})$ can be divided in the following way

$$\omega \equiv \omega_{sym}\, \omega_{pl}\, \omega_r\, \omega_{NCC}\, \omega_{int}, \tag{3.8}$$

where

ω_{sym} is the quantum symmetrization weight factor

$$\omega_{sym}(\mu) \doteq \frac{1}{\prod_{i=1}^{A} \xi_\mu(i)!}, \tag{3.9}$$

where $\xi_\mu(i)$ is the number of clusters of size i in μ. In MMMC77 an approximation of eq. (3.9) is used. In app. B.2.1 the method used in MMMC95 is presented. It is an exact method. Even though ω_{sym} is not explicitely computed it is exactly taken into account in the Metropolis sampling (for an independent and generalized discussion, including charges and continuous variables, see Raduta [RR97]).

ω_{pl} is the result of the integration over the linear and angular momenta

$$\omega_{pl} \propto C(\mu) E_r^{\tilde{N}}, \tag{3.10}$$

where $E_r = E - E_b - E^* = E_k$ is the remaining energy. $C(\mu)$ is only a function of the mass distribution μ, it is proportional to the product of the clusters masses and of the clusters principal moment of inertia; $\tilde{N}$ is the number of translational–rotational dofs divided by two minus one, e.g. for a gas of monomers $\tilde{N} = \frac{3A}{2} - 1$.
At fixed remaining energy E_r, ω_{pl} drives the mass distribution towards an increasing number of translational–rotational dofs, i.e. increasing number of fragments.

ω_r is the weight due to the angular part of the clusters eigen rotation. It depends on the number of rotational dofs.
Results of simulations show that this weight plays no significant role at low pressure (neither qualitatively nor quantitatively), at least for reasonable values of the input parameters, i.e. essentially the value taken by the inertial momenta.

ω_{int} is the factor due to the internal dofs of the clusters. It is the product of the internal degeneracy $\omega_{int,i}$ of each clusters (provided that $N_i > 2$)

$$\omega_{int,i}\left(E_i^*\right) \doteq \exp S_{int}\left(N_i^*, E_i^*\right), \tag{3.11}$$

where $S_{int}\left(N_i^*, E_i^*\right)$ is given by eq. (3.3) on page 43.
As the specific surface entropy at fixed specific internal excitation energy is smaller than the specific volume entropy, ω_{int} tries to form big clusters in opposition with ω_{pl}.

ω_{NCC} is due to the integration over the clusters center of mass $\{\mathbf{r}_1, \ldots, \mathbf{r}_{N_f}\}$, i.e. the number of spatial configurations allowed in the container (no overlap with the boundary or between the clusters is allowed)

$$\omega_{NCC} \doteq \int_V \ldots \int_V d\mathbf{r}_1 \ldots d\mathbf{r}_{N_f} \Theta\left(\mathbf{r}_1, \ldots, \mathbf{r}_{N_f}\right) \eta\left(\mathbf{r}_1, \ldots, \mathbf{r}_{N_f}\right) \tag{3.12a}$$

$$\doteq \frac{V^{N_f}}{NCC}, \tag{3.12b}$$

where Θ forbids the overlapping of a cluster with the boundary

$$\Theta\left(\mathbf{r}_1, \ldots, \mathbf{r}_{N_f}\right) \doteq \begin{cases} 0 & \exists i \text{ such that } |\mathbf{r}_i| > R - R_i, \\ 1 & \text{else.} \end{cases} \tag{3.13}$$

η forbids the overlapping between two clusters

$$\eta\left(\mathbf{r}_1, \ldots, \mathbf{r}_{N_f}\right) \doteq \begin{cases} 0 & \exists i, j \text{ such that } |\mathbf{r}_i - \mathbf{r}_j| < R_i + R_j, \\ 1 & \text{else.} \end{cases} \tag{3.14}$$

NCC is the inverse probability to find a set of positions for the clusters center of mass so that all clusters fit into the container. For very large volumes NCC is close to one. For $N_f > 2$ exact analytical evaluation of NCC is up to now practically impossible. In app. A.1.2 an approximation of NCC is worked out using the equation of state (EOS) of hard-spheres gas [MCSL71]. For $A \approx 500$, this approximation turns out to be relatively good for pressures up to ~ 100 atmospheres [p] (see chap. 4). For higher pressures, estimates of NCC based on EOS which are in their turn only based on two body correlations are useless and NCC has to be evaluated via a Monte–Carlo scheme. The one used in the present work is briefly described in app. A.2.
At low pressures $\omega_{NCC} \approx V^{N_f}$. Hence, this weight drives the system mass in the same direction as ω_{pl}, i.e. towards increasing number of fragments.

The caloric curves presented in sec. 3.4 are mostly the results of a competition between the internal dofs and the translational+positioning ones (the former try to bound the atoms in clusters, whereas the latter prefer as many fragments as possible). Moreover, as discussed in sec. 3.4 two key ingredients for the multifragmentation regime are the shell structure of the clusters reflected in the binding energies and the quantum symmetrization weight ω_{sym}.

Observables

The physical quantities of interest are the averages $\langle F \rangle$ of observables F over the microcanonical ensemble

$$\langle F \rangle \doteq \frac{\int_W F\left(\{\mathbf{q}, \mathbf{p}\}\right) d\mathbf{q}\, d\mathbf{p}}{\int_W d\mathbf{q}\, d\mathbf{p}} \tag{3.15}$$

$$= \frac{\int_{W'} F\left(\mathbf{x}\right) \omega(\mathbf{x})\, d\mathbf{x}}{\int_{W'} \omega(\mathbf{x})\, d\mathbf{x}} \tag{3.16}$$

[p] For a given microcanonical pressure, the approximation becomes better with increasing A, because the relative weights of NCC and its derivatives are less and less important as the system grows $A \to \infty$, $p = cst$, see below.

The Metropolis sampling replaces the integral in eq. (3.16) on the preceding page by a discrete sum

$$\langle F \rangle = \frac{1}{N} \sum_{j=1}^{N} F(\mathbf{x}_j) . \tag{3.17}$$

The energy and volume dependencies of $\omega(\mathbf{x})$ appear explicitly only in ω_{pl} and ω_{NCC}. Thus the system entropy can be written in the following condensed way

$$\begin{aligned} S &= \ln \int_{W'} d\mathbf{x}\, \omega(\mathbf{x}) && (3.18) \\ &= \ln \int_{W'} d\mathbf{x}\, C(\mathbf{x}) \frac{V^{N_f}}{NCC} E_k^{\tilde{N}}, && (3.19) \end{aligned}$$

where V, N_f, NCC, E_k and $\tilde{N}$ depend implicitly on $\mathbf{x}$, $C(\mathbf{x})$ does not depend explicitely on E or on V. The inverse temperature (at constant volume) $\beta \equiv \beta_V$ is defined as

$$\begin{aligned} \beta &\doteq \frac{\partial S}{\partial E} && (3.20) \\ &= \frac{\int d\mathbf{x}\, C(\mathbf{x}) \tilde{N} \frac{V^{N_f}}{NCC} E_k^{\tilde{N}-1}}{\int d\mathbf{x}\, C(\mathbf{x}) \frac{V^{N_f}}{NCC} E_k^{\tilde{N}}} \\ &\equiv \left\langle \frac{\tilde{N}}{E_k} \right\rangle . && (3.21) \end{aligned}$$

The microcanonical pressure p is

$$\begin{aligned} p &\doteq \frac{1}{\beta} \frac{\partial S}{\partial V} && (3.22) \\ &= \frac{1}{\beta} \frac{1}{\int d\mathbf{x}\, \omega(\mathbf{x})} \left[\int d\mathbf{x}\, C(\mathbf{x}) N_f \frac{V^{N_f-1}}{NCC} E_k^{\tilde{N}} - \int d\mathbf{x}\, C(\mathbf{x}) \frac{1}{NCC} \frac{\partial NCC}{\partial V} \frac{V^{N_f}}{NCC} E_k^{\tilde{N}} \right] \\ &\equiv \frac{1}{\beta} \left[\left\langle \frac{N_f}{V} \right\rangle - \left\langle \frac{\partial \ln NCC}{\partial V} \right\rangle \right] && (3.23) \\ &\doteq p_{kin} + p_{NCC}. && (3.24) \end{aligned}$$

where $p_{kin} \doteq \frac{1}{\beta} \left\langle \frac{N_f}{V} \right\rangle$ and $p_{NCC} \doteq -\frac{1}{\beta} \left\langle \frac{\partial \ln NCC}{\partial V} \right\rangle > 0$ are resp. the kinetic and the "avoided volume" or NCC parts of the total pressure p.

Most of the results presented in the next section are shown at constant *microcanonical* pressure. The reasons are that all macroscopic parameters for the liquid–gas transition of sodium are experimentally measured at constant pressure. Furthermore, near the critical point, the pressure is a control parameter for the first and second order phase transitions (see sec. 2.2). Nevertheless, the computations are *not* performed at constant pressure leaving the volume free to fluctuate. But, on the contrary, the volume is *fixed* for each run and slowly adapted from one run to the other in order to reach the desired pressure. This procedure allows one to follow an isobar in the energy–volume plane just like the ones computed for the van der Waals model in sec. 2.2 (see e.g. fig. 1.5(b) on page 15). The uniqueness of this isobar, i.e. that there is only *one* v solution of $p(\epsilon, v) = p_0$ at fixed ϵ, is a priori not guaranteed. Indeed, at small energies and volumes the isobars split up into three branches, see fig. 3.6 on the next page. For a given total specific excitation energy smaller

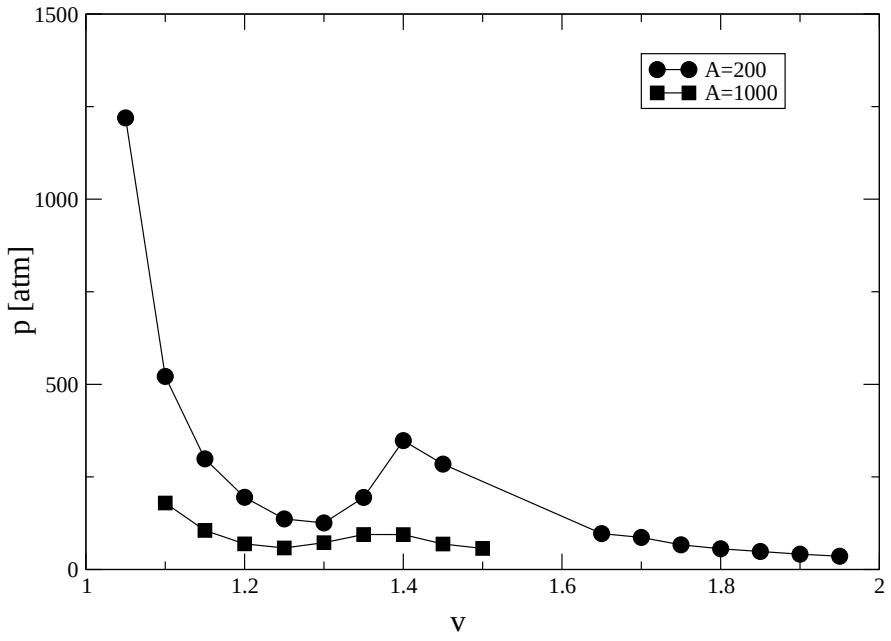

Figure 3.6: Pressure vs normalized volume v at fixed excitation energy $\epsilon \approx 0.2$ eV/atom and for different total masses. At fixed low energy, the equation $p(v) = v_0$ can have three solutions. The mass distribution for the branch with the lowest volume is composed of only one big cluster. As the system volume increases this cluster starts to evaporate some monomers (beginning of the negative compressibility region). The evaporation of the firsts monomers are responsible of this negative compressibility region via p_{NCC}, the avoided volume term in the total microcanonical pressure p (see eq. (3.24)).

than ϵ^*_{max} it is always possible to get the desired pressure by quenching the big cluster in a very small volume (at very low energy this is the only way to reach the appropriate pressure). This branch has very high temperatures, e.g. at $h \approx 0.2$, $T_V \approx 1200$ K. But the volume of the phase space of this solution is small compared to the one with many fragments at large system volume (if this branch is open). There is a third branch between the two above mentioned branches. It is characterized by a positive $\frac{\partial p}{\partial v}|_\epsilon$. In the following, solutions from the branch with the largest volume are plotted. It is the only branch that goes from the gas to the liquid solution when $\epsilon \to 0$ by slow variations of ϵ and v . This effect vanishes in the limit $N \to \infty$, because the difference of the system volumes of these two solutions shrinks. A more satisfactory solution would have been to study the temperature-surface over the *whole* parameter space, i.e. as a function of the "extensive" parameters ϵ and v.

3.4 Results

3.4.1 $\mathbf{N_{a\,200}}$, 1 atm.

On fig. 3.7 on the facing page the results from MMMC95 for $A = 200$ at atmospheric pressure are summarized.

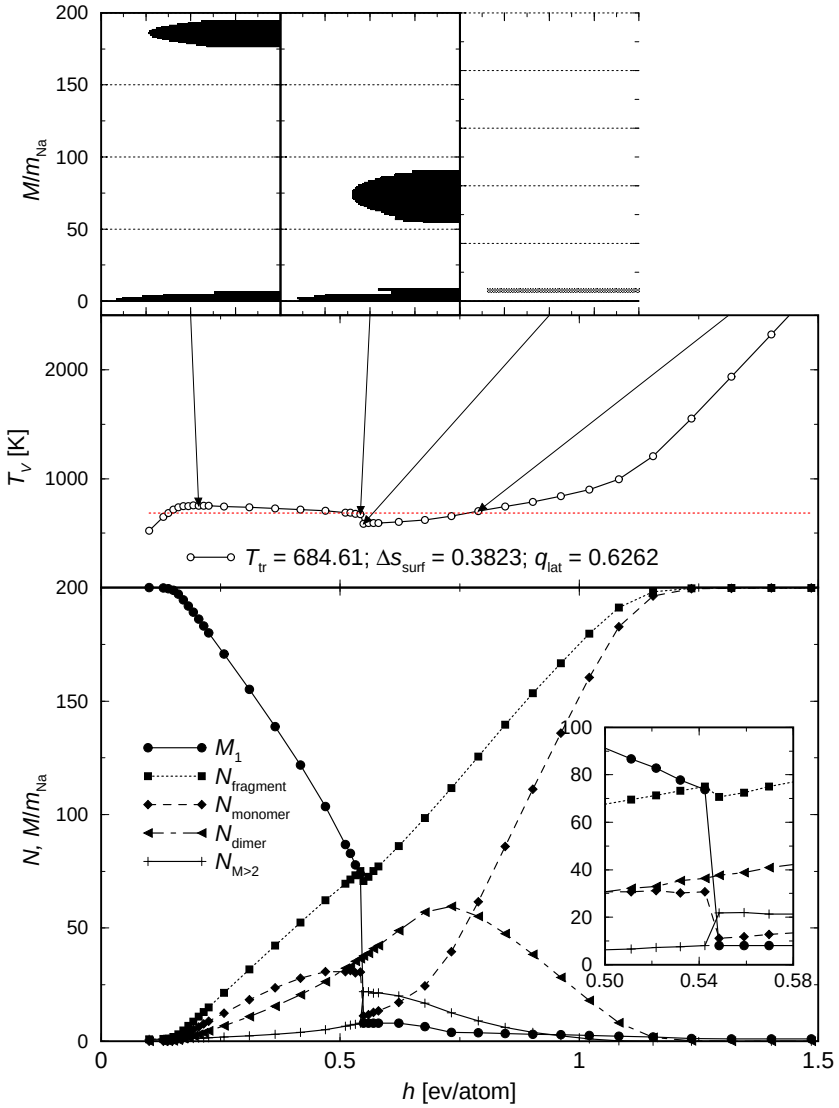
M/m_{Na}
T_V [K]
T_{tr} = 684.61; Δs_{surf} = 0.3823; q_{lat} = 0.6262
N, M/m_{Na}
M_1
$N_{fragment}$
$N_{monomer}$
N_{dimer}
$N_{M>2}$
h [ev/atom]

Caloric curve

On fig. 3.7(e) the isobar $p = 1$ atm is plotted (plain line) in the (h, T_V) plane, where $h = \epsilon + pv$ is the specific enthalpy and T_V the microcanonical temperature [q,r].

There are several distinct enthalpy regions. For $h \lesssim 0.15$ eV/atom T_V increases monotonically; at $h \approx 0.15$ eV/atom T_V starts to be a *decreasing* function of h, i.e. $C_V < 0$ which signals a first order phase transition. T_V decreases quasi–linearly up to $h \approx 0.55$ eV/atom. There it drops down within a small h–range (very low heat capacity). After that, $T_V(h)$ recovers a "normal" behavior (positive heat capacity) with three distinct parts, one for enthalpies within $\approx [0.55, 0.75]$, another [s] for $h \in [0.75, 1.15]$ and the last for $h > 1.15$.

According to sec. 2.2.3 on page 27 one can define transition parameters via the Maxwell construction (dotted line in fig. 3.7(e)). The transition temperature is $T_t \equiv T_{tr} \approx 685$ K, the latent heat $q_{lat} \approx 0.382$ eV/atom and the specific surface entropy $\Delta s_{surf} \approx 0.626$ atom^{-1} (the bulk values are $T_t = 1156$ K, $q_{lat} = 0.923$ eV/atom and the specific surface entropy Δs_{surf} vanishes [FL95]). The behavior of the transition parameters as function of the systems total mass is discussed in sec. 3.4.2.

Mass distribution

Several observables giving information about the mean mass distribution as a function of h are plotted in fig. 3.7 on the page before. In figs. 3.7(a)–(d) the logarithm of $\langle N_j \rangle$ the mean number of fragments of size N_j is plotted (arbitrary scale), at different enthalpies (given by the arrows on fig. 3.7(e)).

In fig. 3.7(f) are plotted: $M_1 \equiv \langle M_1 \rangle$, $N_{fragment} \equiv \langle N_f \rangle$, $N_{monomer} \equiv \langle N_m \rangle$, $N_{dimer} \equiv \langle N_d \rangle$ and $N_{M>2} \equiv \langle N_{M>2} \rangle$ which are respectively the mean mass of the largest fragment, number of fragments, number of monomers, number of dimers and number of fragments bigger than 2, $\langle N_f \rangle = \langle N_m \rangle + \langle N_d \rangle + \langle N_{M>2} \rangle$.

At low enthalpy, $h \lesssim 0.15$, all the atoms are in one big cluster ($\sim$ liquid phase). Starting from $h \approx 0.15 < 0.35 = \epsilon^*_{max}$ up to $h \approx 0.55$ the big cluster size shrinks and light fragments (essentially monomers and dimers) are produced. $\langle N_f \rangle$ is a linear function of h. Here, as the specific heat capacity is negative, there is a first order phase transition, with co-existence of a "liquid" ($\sim$ big cluster) embeded in a "gas" ($\sim$ light fragments). It is an evaporation regime.

Around $h = 0.55$ the mass distribution is completely reorganized within a short h–range (see inset fig. 3.7(g)). From a mass distribution composed by one big "liquid" cluster and a gas of monomers and dimers it changes to a multifragmentation regime with a broad mass distribution of relatively small clusters, $N_j \lesssim 12$ (figs. 3.7(b), (c) and (g)). The dominant fragment sizes are in decreasing order: dimers (2–mers), monomers (1–mers), quadrimers (4–mers), octomers (8–mers). The relative large number of clusters of those

[q]The pv–shift is not very important at atmospheric pressure, i.e. $h_2 - h_1 \approx \epsilon_2 - \epsilon_1$ for two neighboring points on the curve in fig. 3.7(e). One can check that in fig. 3.7(e); there the energy difference $\Delta\epsilon$ between two points (small circles) is $\Delta\epsilon = 0.05$ eV/atom, which is also the difference expressed in h, $\Delta h \approx 0.05$ eV/atom (apart around $\epsilon = 0.55$ and $\epsilon = 0.25$ where smaller energy steps are used).

[r]Each point in the energy–volume plane (represented by a point in fig. 3.7) is the results of the averaging over 2.10^6 events except for $\epsilon \approx 0.25$ and $\epsilon \approx 0.55$ where higher statistics (up to 20.10^6 events) are used in order to ensure stable results. The statistical errors due to the Monte–Carlo averaging for the temperature and the mass distribution curves are below 1 %. The convergence of the results has been check by starting from several initial conditions and also by studying intermediate averages in very long run.

[s]Due to the temperature scale in fig. 3.7(e), it is difficult to distinguish the two first parts; they can be better seen in fig. 3.17 on page 64.

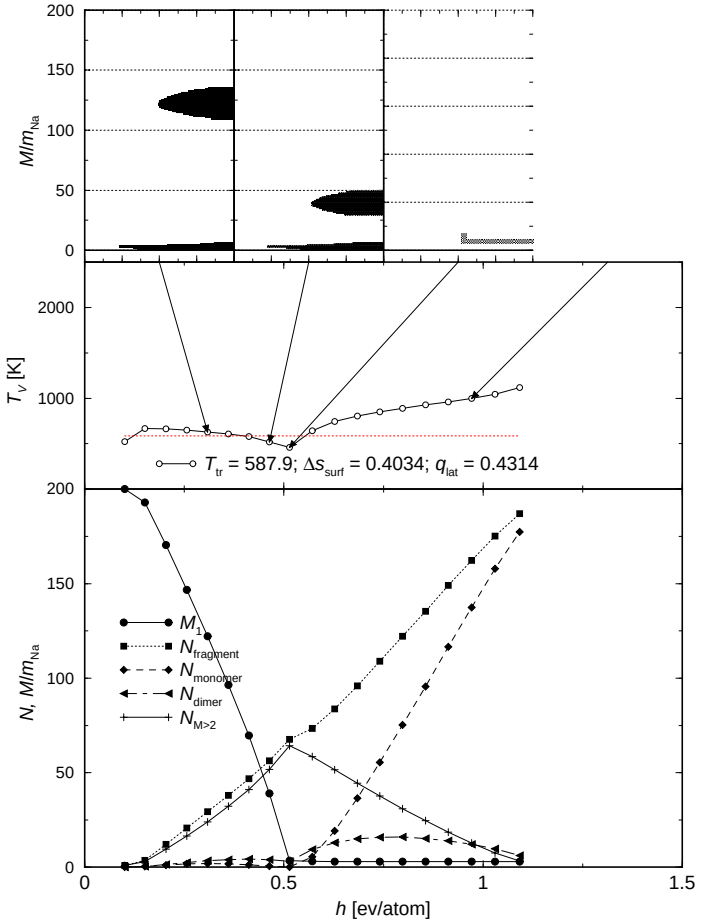
200
150
100
50
0
M/m_Na
2000
1000
T_v [K]
T_tr = 587.9; Δs_surf = 0.4034; q_lat = 0.4314
200
150
100
50
0
N, M/m_Na
M_1
N_fragment
N_monomer
N_dimer
N_M>2
0
0.5
1
1.5
h [ev/atom]

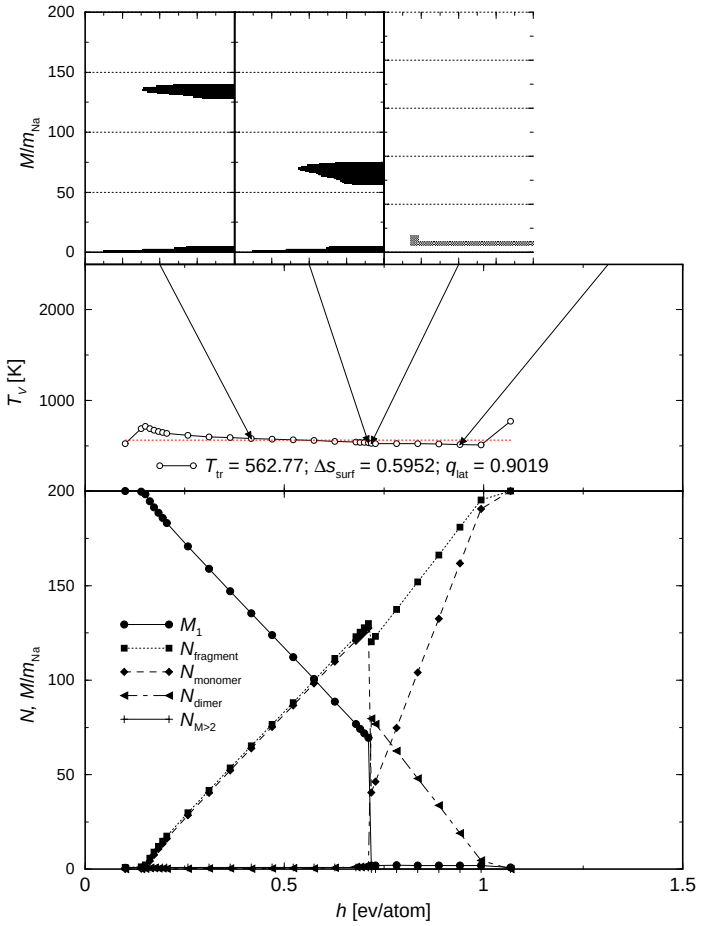
200
150
100
50
0
M/m_Na
2000
1000
T_V [K]
T_tr = 562.77; Δs_surf = 0.5952; q_lat = 0.9019
200
150
100
50
0
N, M/m_Na
M_1
N_fragment
N_monomer
N_dimer
N_M>2
0
0.5
1
1.5
h [ev/atom]

fixed specific internal energy), due to the fading of surface effects with increasing cluster size, one can already predict that the multifragmentation transition is more and more delayed (shifted to higher h) with increasing A.

During this fast transition (from an evaporation regime to a multifragmentation one) the number of monomers decreases from 30 to 10. From $h = 0.55$ the number of fragments bigger than 2 and the mass of the biggest one steadily decrease, while the number of monomers constinuously increases up to eventually a complete gas of monomers for $h \gtrsim 1.15$. However between $h \in [0.55, 0.75]$ the dimers are the dominant fragments, the mean number of dimers even increases within this range (see fig. 3.7(e)).

Surface tension γ

As already written in sec. 2.2.3 the depth of the convex intruder in the specific entropy Δs_{surf} can be linked to the surface tension γ by

$$\gamma = T_t \frac{A \Delta s_{surf}}{\mathcal{A}}, \tag{3.25}$$

where $\mathcal{A}$ is the interphase surface area, T_t the transition temperature defined by the Maxwell line and A the system total number of atoms.

Gross and Madjet have presented in [GM97] the first successful microscopic calculation of the surface tension γ in liquid sodium (and other metals) at atmospheric pressure. The principal obstacle towards an estimate of γ is the definition and estimate of $\mathcal{A}$ (see discussion in sec. 2.2.3 in part I). In [GM97] the authors proposed the total surface area of the fragments of total mass bigger than 1 as a measure of $\mathcal{A}$. This area is proportional to N_{eff}, the effective number of surface atoms

$$N_{\text{eff}} = \sum_{j=2}^{A} j^{2/3} \xi_\mu(j), \tag{3.26}$$

where $\xi(j)$ is the mean number of clusters of size j in the mass distribution μ. The interphase surface area is given by

$$\mathcal{A} = 4\pi r_w^2 N_{\text{eff}}, \tag{3.27}$$

where r_w is the Wigner–Seitz radius.

In [GM97] N_{eff} is approximatively constant in the evaporation region for $A = 200$ and $A = 3000$ (see fig.1 in [GM97]), then it increases abruptly at the beginning of the multifragmentation. Finally it decreases and eventually vanishes in the gas phase. In [GM97] the value of N_{eff} used in eq. (3.27) to estimate the surface tension (or to be more precise the surface tension parameter divided by the transition temperature $\frac{\sigma}{T_t} = 4\pi r_w^2 \frac{\gamma}{T_t} = \Delta s_{surf} \frac{A}{N_{\text{eff}}}$) is the average of N_{eff} over the evaporation region.

In the new simulations N_{eff} is not constant at all for either $A = 200$ or $A = 1000$ (see figs 3.10 and 3.11 on the next page) or for any other studied system size. For $A = 200$, N_{eff} is an increasing function in the evaporation region and *also* in the multifragmentation one for $h < 0.75$. This is due to the huge ongoing production of 2–mers up to $h = 0.75$ (see fig. 3.7 on page 51). This can be verified in fig. 3.10 where N_{eff} has been plotted for another definition, i.e. the same as the one given by eq. (3.26), but the sum goes from 4 to A (instead of 2 to A). The qualitative behavior of this new N_{eff} is similar to the one of N_{eff}

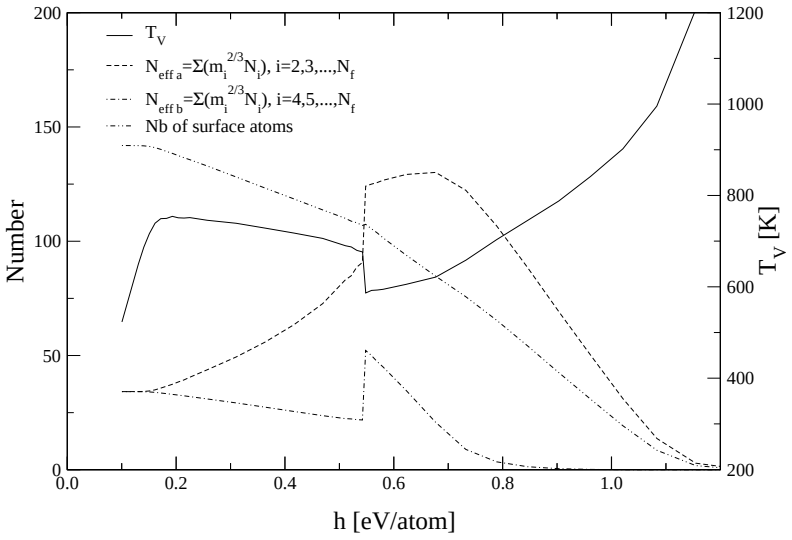

Figure 3.10: Effective number of surface atoms N_{eff} based on different definitions ($A = 200$) and microcanonical temperature T_V (solid line). The definitions for N_{eff} are (a) $N_{\text{eff}\,a} = \sum_{i=2}^{N_f} i^{2/3}\xi(i)$ (dashed line), (b) $N_{\text{eff}\,b} = \sum_{i=4}^{N_f} i^{2/3}\xi(i)$ (point-dashed line) and (c) the number of surface atoms $N_{\text{eff}\,c} = N_s^*$ as defined by eqs. 3.4a and 3.4b on page 43 (point-point-dashed line). $N_{\text{eff}\,b} - N_{\text{eff}\,a}$ gives simply the 2–mers contribution since $\langle N_d \rangle \gg \langle N_t \rangle$ (see fig. 3.7). $N_{\text{eff}\,a}$ increases up to $h = 0.75$, i.e. even in the multifragmentation regime (this is a consequence of the 2–mers production see fig. 3.7) while $N_{\text{eff}\,b}$ steadily decreases apart at $h \approx 0.55$ where it suddenly jumps because of the production of many 8–mers and 4–mers.

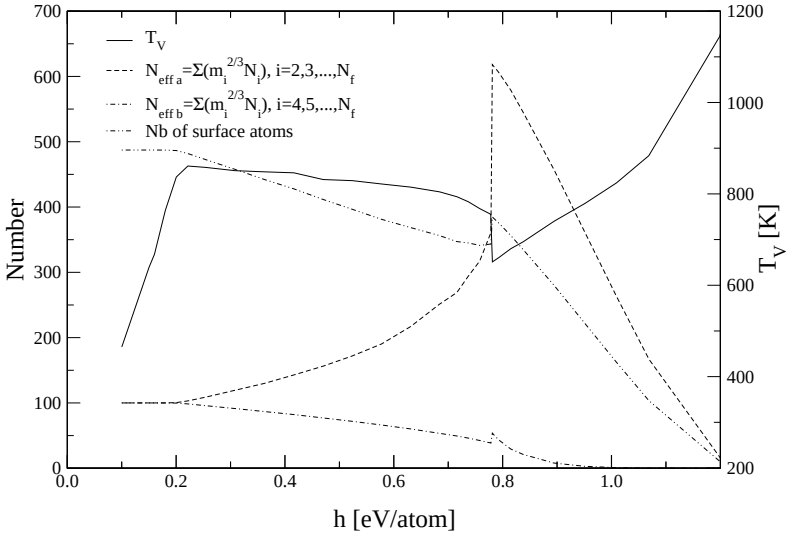

Figure 3.11: Same as fig. 3.10 but for $A = 1000$. $N_{\text{eff}\,a}$ does no longer increase in the multifragmentation regime. The contribution of the 2–mers to $N_{\text{eff}\,a}$, i.e. $N_{\text{eff}\,b} - N_{\text{eff}\,a}$ is even more important than for $A = 200$.

presented in [GM97], hence by analogy and also by considering that the 2–mers and the 3–mers can be regarded as members of the vapor, it is the average over the evaporation region of the new N_{eff} that is used in the rest of this section to estimate the interphase surface area. And the results are for $A = 200$

$$\begin{aligned} N_{\text{eff}} &= 29.3 \\ \frac{\sigma}{T_t} &= 2.61. \end{aligned}$$

The bulk values are $N_{\text{eff}} = \infty$ and $\frac{\sigma}{T_t} = 7.41$ [GM97].

Clearly these results suffer from the ambiguity of the definition of the surface area, and as any other "reasonable" definition the one used here is rather arbitrary (see discussion in sec. 2.2.3). Hence the error bars on $\frac{\sigma}{T_t}$ are big. Nevertheless one can see that microscopic computations give at least the order of magnitude of the transition parameters. For increasing system size these estimates become better, see sec. 3.4.2 where the scaling properties of the transition parameters (including $\frac{\sigma}{T_t}$) are discussed.

Comparison with [GM97]

As already noticed there are some differences between the results for the liquid–gas phase transition of small sodium clusters presented here and the one by Gross and Madjet published in [GM97]. In the following the origins of some of these differences are discussed and explained.

In fig. 3.12 a summary of the results obtained from MMMC77 for $\mathrm{N_{a\,200}}$ is shown [GM97, GROA].

First, note that the temperature plotted is not $T_V(h)$ but the microcanonical temperature at *fixed pressure* $T_p(\epsilon) \doteq \beta_p^{-1}(\epsilon)$, where

$$\beta_p \doteq \frac{\partial S}{\partial E}|_p \tag{3.28}$$

$$= \beta_V \left[1 - p \frac{\frac{\partial p}{\partial E}|_V}{\frac{\partial p}{\partial V}|_E} \right], \tag{3.29}$$

where p is the microcanonical pressure (see app. D). For small pressure $\beta_p > \beta_V \Leftrightarrow T_p < T_V$. As the pv–shift is not very important at atmospheric pressure (see footnote q on page 52) one can use alternatively ϵ or h as a parameter (although h is the correct one according to standard thermodynamics). But the choice of T_p as an observable changes clearly the value of the transition parameters. In practice as it is shown below, in the transition region, the caloric curves T_p are simply shifted vertically compared to T_V curves, i.e. $T_p \approx T_V - K$, where K is a positive constant (K is of the order of 150 Kelvin for $A = 200$).

The results in fig. 3.12 are qualitatively comparable with the ones shown in fig. 3.7 on page 51. The main qualitative difference is the absence in MMMC95 of the "second" transition from dimers to monomers at $\epsilon^* \approx 1.1$ eV/atom in fig. 3.12. This transition has two origins. The first one is a missing move in the algorithm of MMMC77. To be more precise MMMC77 proposes the move

$$2 \to 1 + 1, \tag{3.30}$$

"splitting of a dimer" but not its inverse ($1 + 1 \to 2$). This missing move breaks "locally" the detailed balance condition (see app. B). At $\epsilon^* \approx 1.1$ there are mainly dimers and

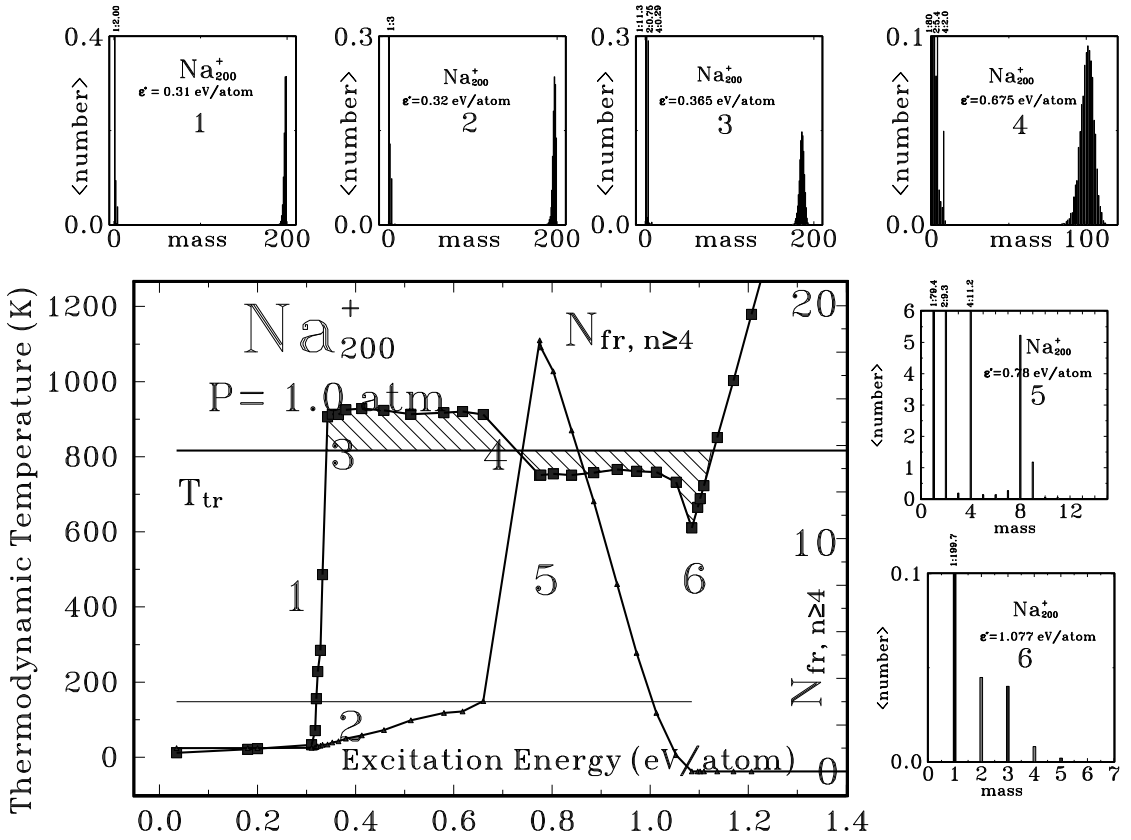

Figure 3.12: $N_{a\,200}$ at 1 atm from [GM97, GROA]. Microcanonical temperature at *constant pressure* (square) as a function of the excitation energy ϵ^*, number of fragments of mass bigger than 3 (triangle) and Maxwell line. The small figures show the mass distribution of fragments at six different ϵ^* which are indicated in the main figure by their number. The small vertical numbers on the top of the mass distribution give the real number of fragments, e.g. 2 : 9.3 means there are on the average 9.3 dimers at $\epsilon^* = 0.78$ eV/atom.

monomers, so if the move $2 \to 1+1$ is accepted, the simplest ("shortest") way to go back is the following chain of successive moves

$$\begin{aligned} 1+2 &\to 3, \\ 1+3 &\to 4, \\ 4 &\to 2+2. \end{aligned}$$

But as it is suggested by the small number of trimers and 4–mers, the probability of occurrence of this chain of events is very small. Hence at $\epsilon^* \approx 1.1$ once a dimer is split up into two monomers the monomers remain as they are for the rest of the MMMC77 run. Thus MMMC77 produces more monomer than it should. This abnormal increase of the number of particles cools down the system.

The second explanation for the lack of second transition is the choice of T_p as observable as it is shown below.

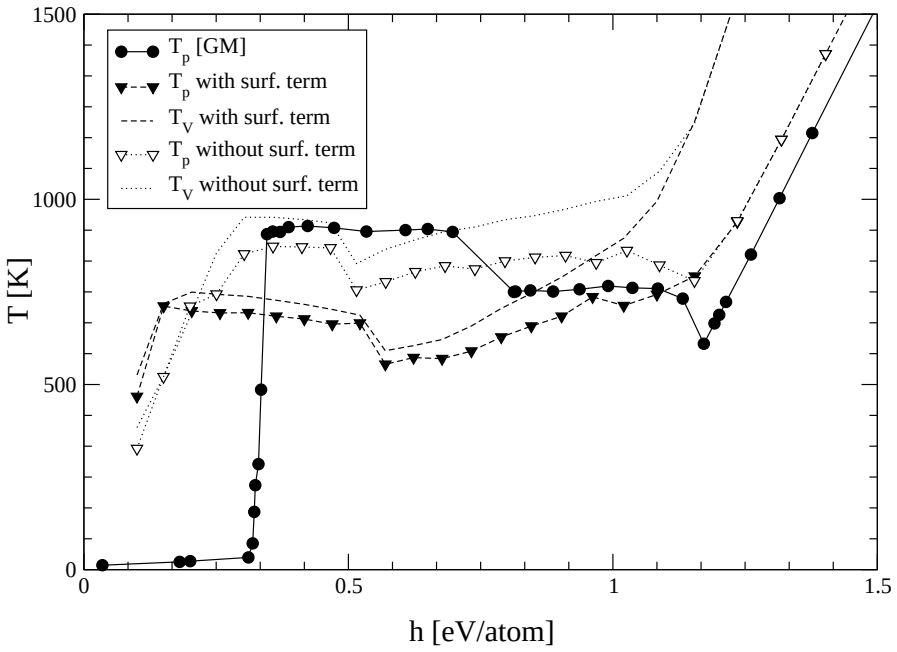

Figure 3.13: $N_{a\,200}$. Temperature at fixed pressure T_p from [GM]≡[GM97] (solid line, circles), from the present work (triangles) and temperatures at fixed volume T_V (no symbol) as functions of the specific enthalpy h. The two latter temperatures are plotted for MMMC with surface entropy term for the cluster internal entropy (dashed line) and without this surface term (dotted line). Note that the statistical errors on T_p are larger than the one on T_V since T_p relies on the estimate of second order derivatives of S (see app. D). These errors are of the order of 10 % → ±80 K toward $h = 1.1$ eV/atom. The "second" phase transition in T_p [GM] can only merely be seen in T_p without surface term and is completely absent in the other curves from MMMC95.

To unable qualitative comparisons, different temperature curves from several models are plotted in fig. 3.13. First the solid line with circles reproduces the T_p curve from fig. 3.12, but now T_p is a function of h. The other curves represent temperatures from MMMC95. The ones with symbols are microcanonical temperatures at constant volume T_V and the curves without symbols are microcanonical temperatures at constant pressure T_p. The dashed lines reproduce the results from fig. 3.7 on page 51. One of the major difference between the two MMMC models is the presence of a surface entropy term for clusters entropy in MMMC95 (see sec. 3.2 and eq. (3.3) on page 43). So in order to emphasize the role of this surface term the temperature curves (T_V and T_p) from MMMC95 but *without* surface terms [t] are also plotted in fig. 3.13 (dotted lines). One can find a summary of the results for the model without surface term in fig. 3.14 on the next page.

Compared to MMMC77, in MMMC95 the evaporation starts earlier [u]. This is because of the internal entropy model, since in the new version the specific entropy is smaller than in

[t] This is simply achieved by setting N_v^* the number of volume "atoms" to $N^* = N - 2$ the cluster total number of "atoms" in eqs.(3.3) and (3.4) on page 43.

[u] It occurs well below the imposed limit in the internal excitation energy at $\epsilon^* = \epsilon^*_{max} = 0.35$ eV/atom, see item 3 on page 41. This is in contrast with MMMC77 where the transition starts at ϵ^*_{max} for any system size A (see figs. 3 and 4 in [GM97]).

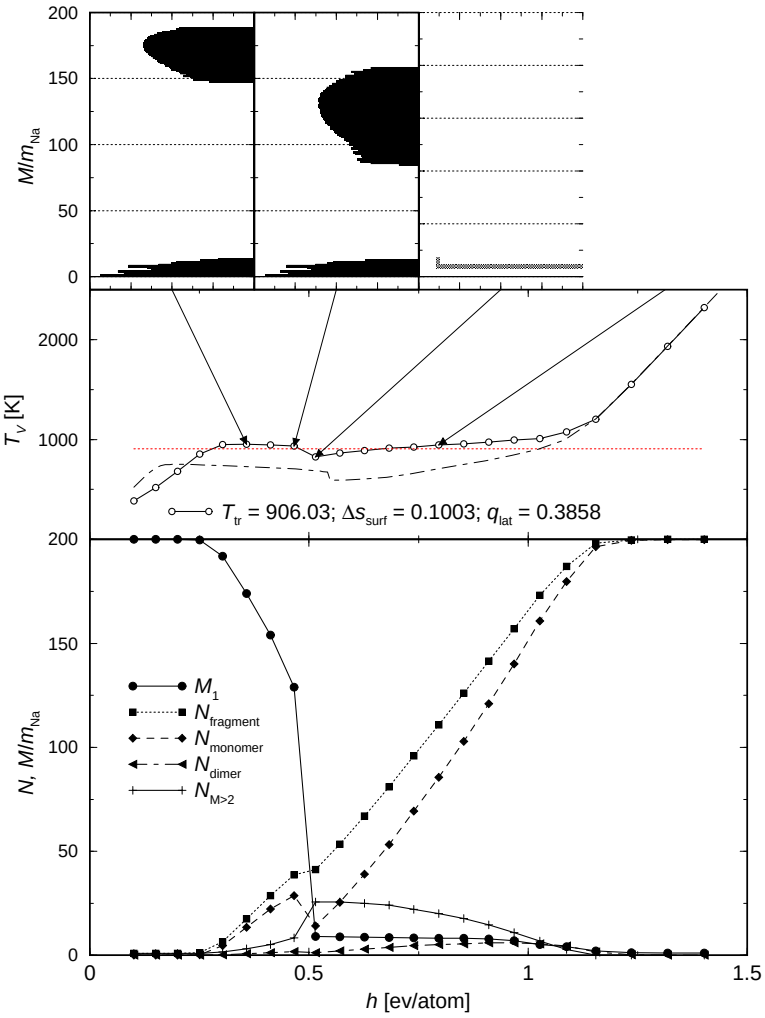
200
150
100
50
0
M/m_Na
2000
1000
T_v [K]
T_tr = 906.03; Δs_surf = 0.1003; q_lat = 0.3858
200
150
100
50
0
N, M/m_Na
M_1
N_fragment
N_monomer
N_dimer
N_M>2
0
0.5
1
1.5
h [ev/atom]

Hence as the specific entropy of a fragment is smaller the big cluster starts to evaporate monomers much earlier ($h \approx 0.35$ in MMMC77 compared to $h \approx 0.15$ in MMMC95). This leads to a larger number of translational-rotational dofs which in its turn cools the system down. One can check this argument in fig. 3.14.

The multifragmentation occurs also at smaller h in MMMC95, but this time the difference of specific internal entropy cannot be invoked since as one can see on fig. 3.13 and 3.14 a higher specific entropy implies an even earlier start of the multifragmentation. Here an explanation for this fact is that contrary to MMMC77, in MMMC95 each cluster has its own internal energy (item 3 on page 41), thus at fixed overall internal energy the system has more dofs in MMMC95 than in MMMC77 due to the partitioning of the excitation energy among the clusters.

In the gas phase the temperature curves are shifted to lower h in MMMC95 compared to MMMC77 ($\Delta h \approx 0.1$ eV/atom). This comes from the fact that the ground state binding energy in MMMC95 is higher than in MMMC77 (~ -180 eV compared to ~ -199 eV), due to a slight changes in the input parameter values of the metal–drop model for the binding energies (i.e. a_v and a_s).

3.4.2 Scaling properties

In fig. 3.15 a summary of the results for $A = 1000$ at atmospheric pressure is plotted. The overall qualitative behavior is similar than for $A = 200$. The main quantitative differences are

- Essentially because of the increase of the cluster specific internal entropy at fixed ϵ^* with cluster size, the evaporation starts later, $h \sim 0.2$. Hence the overall evaporation region takes place at higher temperatures.

- The multifragmentation is also shifted to higher enthalpies. The reasons are first, again the increase of the specific internal entropy, second the lower sensitivity of the system to the symmetrization weight factor (compared with $\omega_{NCC} \sim V^{N_f}$ and $\omega_{pl} \sim E_r^{\tilde{N}}$) and finally the relatively smallest gain in energy due to binding energy of small clusters. The two latter arguments induce a decrease in the number of clusters bigger than one in the gas part of the mass distribution. This favors an larger number of the number of monomers which now dominate the mass distribution over almost all the enthalpy range (except of course at very low energy and in a tiny region around $h = 0.8$, see fig. 3.15(g)).

- The relative fluctuations of the size of the big liquid cluster are smaller than for $A = 200$ (compare figs. 3.7(a)–(b) and figs. 3.15(a)–(b)).

As a consequence of the above second point, the length of the evaporation region gets longer relatively to the one of the multifragmentation regime (for $A = 200$ the ratio of the former h–length to the later is ~ 0.6 see fig. 3.7 whereas for $A = 1000$ this ratio is about 1.4).

The relative weight of p_{NCC} the "avoided volume" pressure in the total pressure $p = p_{kin} + p_{NCC}$ where p_{kin} is the usual kinetic pressure (see sec. 3.3 and eq. (3.24) on page 49) is plotted on fig. 3.16. At atmospheric pressure the contribution from p_{NCC} can be neglected except at very low enthalpies; there a small volume is needed because almost all the excitation energy is absorbed by the internal dofs of the liquid cluster. With increasing

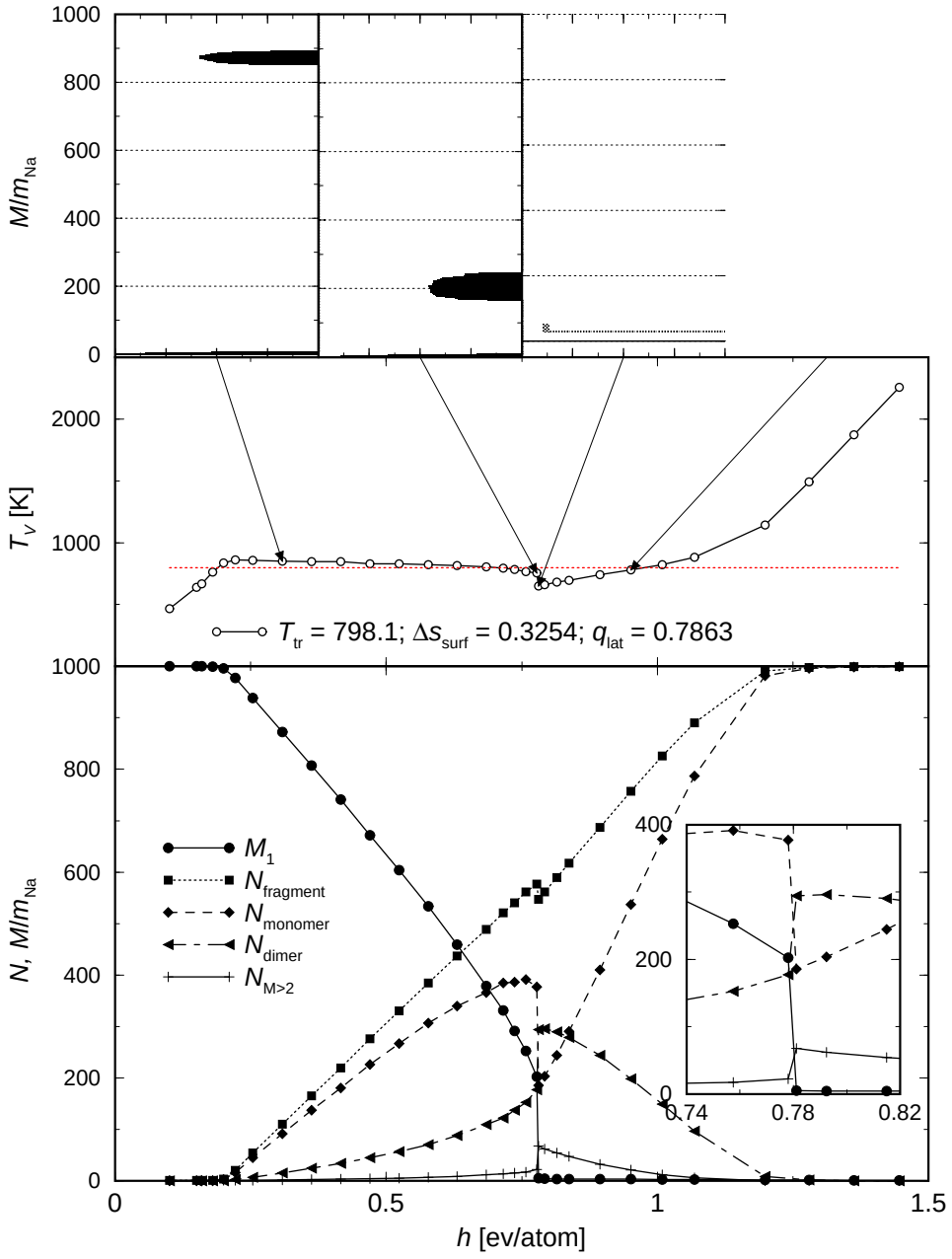
1000
800
600
400
200
0
M/m_{Na}
2000
1000
T_V [K]
T_{tr} = 798.1; Δs_{surf} = 0.3254; q_{lat} = 0.7863
1000
800
600
400
200
0
N, M/m_{Na}
M_1
$N_{fragment}$
$N_{monomer}$
N_{dimer}
$N_{M>2}$
400
200
0
0.74
0.78
0.82
0
0.5
1
1.5
h [ev/atom]

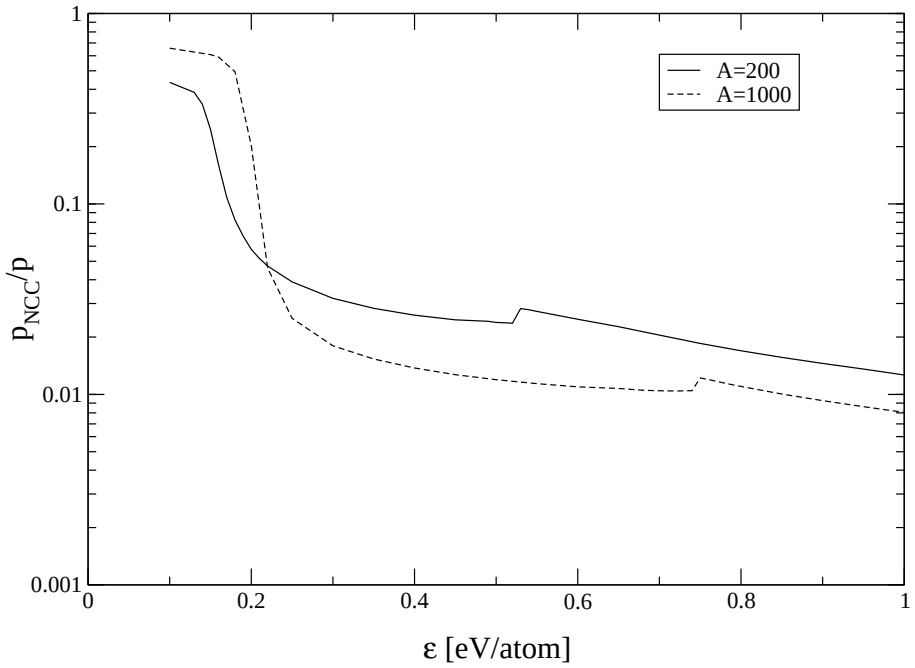

Figure 3.16: Relative weight of p_{NCC} in the total pressure versus ϵ for $A = 200$ (plain line) and $A = 1000$ (dashed line). p_{NCC} is the pressure term coming from the avoided volume. At low pressures p_{NCC} can be neglected apart at very low enthalpies where there is only one cluster. p_{NCC} gets more negligible as A increases.

system size p_{NCC} is more and more negligible as soon as there are more than one fragment in the system; there, at the thermodynamical limit $p_{NCC} = 0$.

In fig. 3.17 the microcanonical temperature (at fixed volume) are plotted as a function of the specific enthalpy and for several system total sizes (from $A = 50$ up to $A = 5000$). One can see a tendency towards the bulk limit even though for $A = 5000$ the curve is still far away from this limit [v]. The specific length of the multifragmentation region gets short with increasing A and eventually vanishes at the thermodynamical limit.

The transition parameters as functions of the system total size A are given in table 3.2 and shown in fig. 3.18 on page 66. They all clearly tend towards their bulk values (as already suggested by the temperatures curves in fig. 3.17). However the specific surface entropy is an increasing of A for $A \lesssim 500$. Hence for $A \lesssim 500$ the system is far from having reach a "scaling behavior" where the specific surface effects would simply vanish as $A^{-1/3}$.

To emphasize the influence of the internal entropy surface term in the cluster entropy model (eq. (3.3)), the transitions parameters for the model *without* this surface term are given in table 3.3. As in table 3.2 they also show a clear trend towards their values at the thermodynamical limit. The notable difference with the results presented in table 3.2 is the very low values of the surface entropy depth Δs_{surf} and hence of σ/T_t. This is due mainly to the very early occurrence of the multifragmentation and the relatively short

[v] Remember that the proportion of surface "atoms" for $N^* = 5000$ is still around 35 %, see fig. 3.5 on page 45.

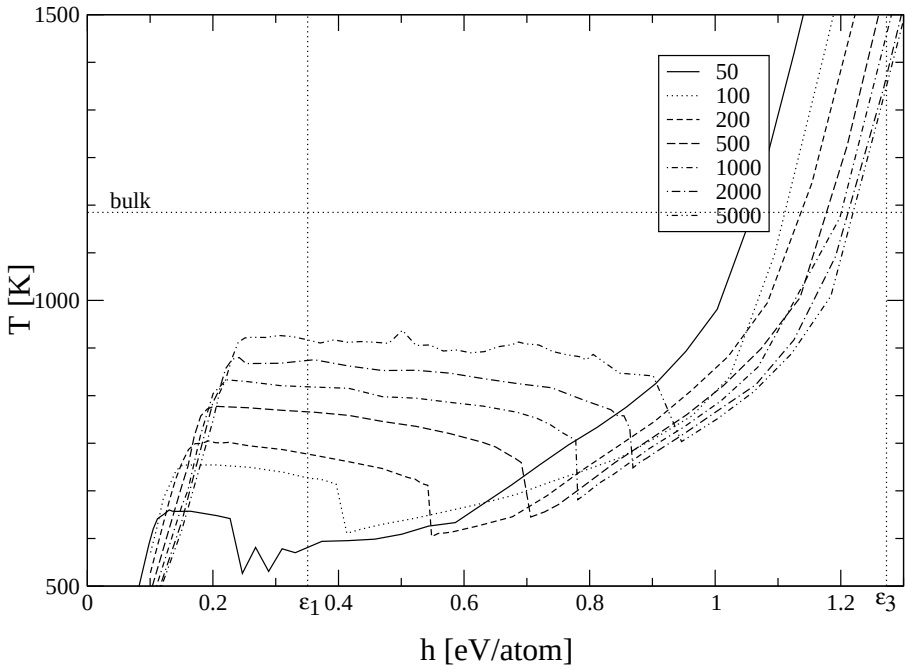

Figure 3.17: Caloric curves versus h for several system total masses, form $A = 50$ up to $A = 5000$. The bulk transition temperature ($T_{t\,bulk} = 1156$ K) is indicated by the horizontal doted line. $\epsilon_1 \approx h_1$ ($\epsilon_3 \approx h_3$) is the specific energy at which the bulk liquid–gas phase transition starts (ends). For $A \lesssim 1000$ the statistical error on the temperature estimate is for each point below 1 %. Above $A \approx 1000$ this error grows rapidly with A: at $A = 5000$ it is about 5 %. Thus the "structures" at the beginning of the multifragmentation for $A = 50$ are not due to statistical fluctuations. Each sudden drops of the temperature in the multifragmentation region corresponds to the fragmentation of a 8–mers.

evaporation region and also to the slightly different mass distributions [w] which induces higher temperature in the multifragmentation regime.

3.5 Summary

Although the cluster model and the numerical code have changed the overall qualitative pictures of the liquid-gas phase transition of sodium clusters at atmospheric pressures, as given in [GM97], is confirmed (apart the "second" phase transition at high enthalpies). From very low enthalpies up to very high ones there are: first a big liquid cluster, then an evaporation regime (the big cluster evaporates very light fragment). This evaporation is eventually followed by a complete reorganization of the mass distribution (multifragmentation) over a small enthalpy range. Then, there is again an evaporation regime or multifragmentation regime (from intermediate cluster masses to monomers). Finally, at high enthalpies the system is a gas of monomers.

According to the definitions of phases and phase transition given in chapter 2, only the

[w] without surface terms there are in the mean less fragments; the monomers are bounded in bigger clusters, e.g. 8–, 4– and 2–mers, see figs. 3.7 and 3.14

A	50	100	200	500	1000	2000	5000	**bulk**
T_t	584.5	659.9	684.6	752.7	799.1	842.4	891.5	**1156**
q_{lat}	0.370	0.557	0.626	0.723	0.786	0.843	0.871	**0.923**
s_{boil}	7.34	9.80	10.62	11.14	11.43	11.62	11.34	**9.267**
Δs_{surf}	0.165	0.278	0.383	0.358	0.327	0.287	0.291	
N_{eff}	13.3	20.5	29.3	48.6	74.7	105	219	∞
σ/T_t	0.09	1.35	2.61	3.65	4.38	5.47	6.63	**7.41**

Table 3.2: Scaling of the transition parameters deduced from the Maxwell construction (cluster internal entropy with surface term). T_t, q_{lat}, s_{boil}, Δs_{surf}, N_{eff} and σ/T_t are the transition temperature, the latent heat, the entropy gain of an evaporated atom $s_{boil} = \frac{q_{lat}}{T_t}$, the entropy surface, the effective number of interphase atoms and the ratio of the surface tension parameter σ to the transition temperature T_t, respectively. The experimental bulk values are given in the last column.

A	50	100	200	500	1000	2000	**bulk**
T_t	750	843	911	960	985	1010	**1156**
q_{lat}	0.154	0.252	0.401	0.638	0.673	0.750	**0.923**
s_{boil}	2.38	3.46	5.11	7.71	7.93	8.61	**9.267**
Δs_{surf}	0.0836	0.103	0.103	0.0846	0.0790	0.0840	
N_{eff}	16.8	25.6	39.3	77	124	209	∞
σ/T_t	0.249	0.40	0.524	0.549	0.637	0.803	**7.41**

Table 3.3: Scaling of the transition parameters given by the Maxwell construction (cluster internal entropy without surface term), see table 3.2.

first evaporation and the multifragmentation are phase transitions, at least in the energy direction. For a complete picture, it is necessary to study the entropy and its derivatives in the energy-volume plane. It is not excluded that the multifragmentation regime (i.e. evaporation of intermediate cluster sizes), corresponds to a phase transition in the *volume* direction.

The influence of different parameters has been studied in this chapter.

Only the quantitative behavior is affected by "reasonnable" choices for the clusters internal entropy. In order to choose among these models for the internal entropies, experimental inputs are needed.

The main factors which lead the system to the multifragmentation regime are the symmetrization weight factor and the electronic shell effects. Thus, the confidence on the prediction of the presence of this regime (for systems at equilibrium) is good, because these factors are well established physical facts (theoretically and experimentally). However, at this moment, the cluster experiments are to rough in order to make any comparison with the present model, see e.g. [SKvIH98].

In this chapter it is shown how and why the multifragmentation vanish at the thermodynamical limit. Hence, the microcanonical thermodynamics allows one to have access to physical phenomenons that do not exist at this limit. The multifragmentation regime is only hardly accessible to a canonical computation. Indeed, its associated temperature is

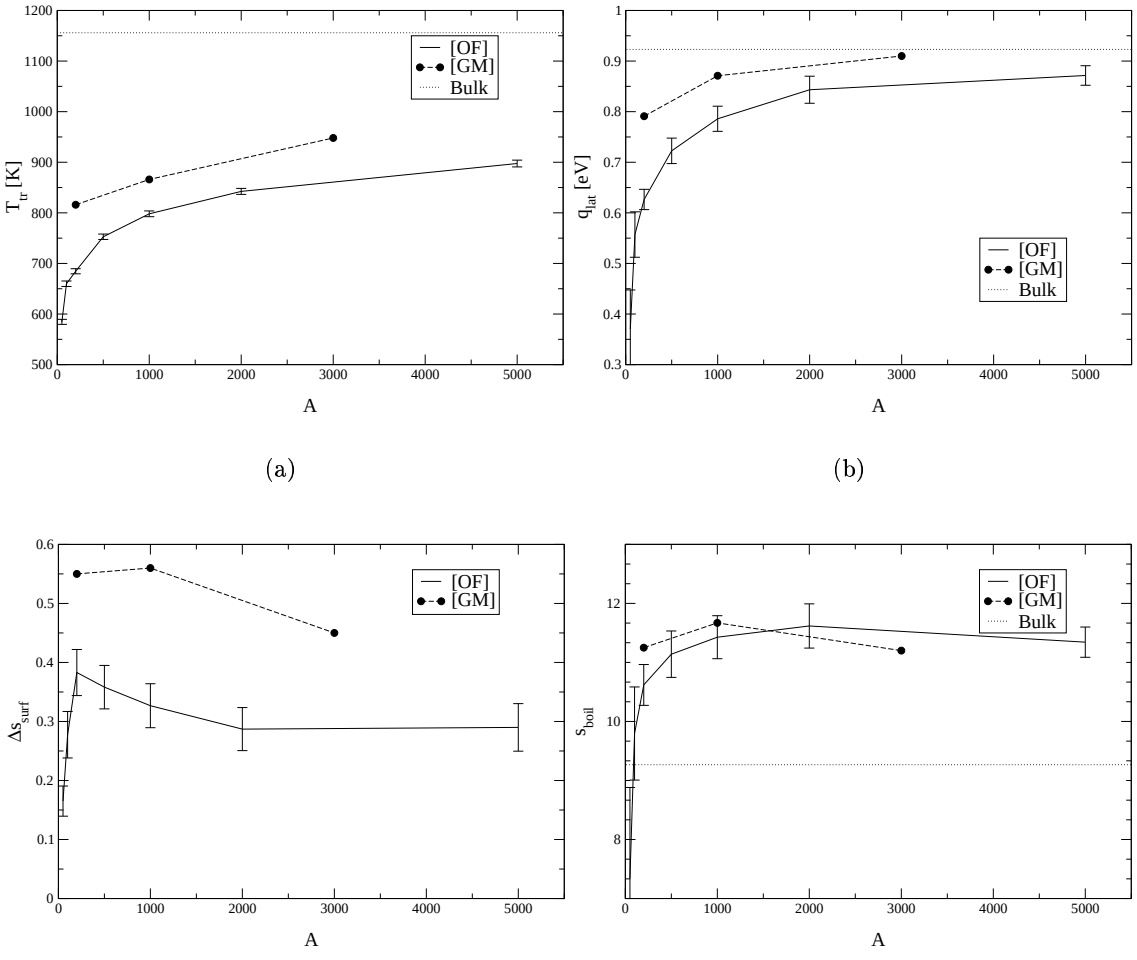

Figure 3.18: Scaling of some transition parameters. (a) Transition temperature $T_t \equiv T_t$. (b) Latent heat q_{lat}. (c) Specific surface entropy Δs_{surf}. (d) Entropy gain of an evaporated atom $s_{boil} \doteq \frac{q_{lat}}{T_t}$. On each panel the results from [GM]≡[GM97] (dashed line) and from the present work [OF] (plain line) are plotted along with the resp. bulk value (dotted line). The error bars for [OF] are estimated granted the fact that the fluctuations of the temperature are of the order of 1 % (this is not the case for $A = 5000$, for this system size the error bars are here underestimated by a factor ~ 2, see fig. 3.17 on page 64).

in the transition region (defined by the Maxwell construction). Therefore, these points do not correspond to global maxima of the Laplace transform, or, to use, the usual "canonical" vocabulary, they do not correspond to minima of the free energy.

Microcanonical thermostatistics offers an efficient way to estimate the surface entropy without imposing any a priori geometry to the surfaces. But the definition of the surface itself area is ambiguous for the present cluster model. Hence, the numerical values for the values of the surface tension parameters presented in this chapter have big error bars. Nevertheless, for systems composed of only a few hundreds of particles, the order of

magnitude of the bulk value is already reached.